nanomanufacturing

MDPI

Article

Performance of SLA Resins Containing Graphene Oxide and Fractionated Kraft Lignin

Rogerio Ramos de Sousa Junior [1,*], Guilherme Elias Saltarelli Garcia [1], Laura Gouveia de Freitas [2], Daniel Florencio de Aquino Faria [3], Gustavo Ryoo Oliveira de Andrade Tanobe [4], Wilson Souza da Silva [1] and Demetrio Jackson dos Santos [1,*]

[1] Center of Engineering, Modeling and Applied Social Sciences, Federal University of ABC (UFABC), Santo Andre 09210-580, Brazil; guilherme.elias@ufabc.edu.br (G.E.S.G.); wilson.souza@ufabc.edu.br (W.S.d.S.)
[2] Nanoscience and Advanced Materials Graduate Program (PPG-Nano), Federal University of ABC (UFABC), Santo Andre 09210-580, Brazil; laura.g@ufabc.edu.br
[3] Electrical Engineering Graduate Program (PPGEEL), Federal University of ABC (UFABC), Santo Andre 09210-580, Brazil; daniel.faquino@ufabc.edu.br
[4] Research, Development & Innovation Department, Suzano Papel e Celulose SA, Suzano 13486-000, Brazil; gtanobe@suzano.com.br
* Correspondence: rogerio.sousa@ufabc.edu.br (R.R.d.S.J.); demetrio.santos@ufabc.edu.br (D.J.d.S.)

Abstract

Additive manufacturing by stereolithography (SLA) is widely used for fabricating complex polymeric parts. However, photocurable resins typically exhibit brittle behavior. In this context, the incorporation of nanofillers has emerged as a strategy to tailor mechanical performance, although challenges related to dispersion and processability remain. This work investigates the co-incorporation of graphene oxide (GO) and kraft lignin, including a low-molecular-weight fraction (FKL), into acrylate-based photocurable resins processed by SLA. Pre-curing dispersion and viscosity were evaluated by optical microscopy and rotational rheometry. The mechanical, viscoelastic, and fracture behavior of the printed nanocomposites was assessed by tensile testing, dynamic mechanical analysis, and scanning electron microscopy. The results show that all formulations exhibited viscosities suitable for SLA processing. The presence of FKL promoted improved GO dispersion and more stable rheological behavior compared with unfractionated lignin. At low lignin contents, a pronounced synergistic effect with GO led to enhanced tensile strength, whereas increasing lignin content reduced stiffness and glass transition temperature while significantly increasing elongation at break, particularly for FKL-based systems. Overall, these findings demonstrate that lignin fractionation is an effective strategy to modulate dispersion, mechanical response, and toughness in GO-containing photocurable resins.

Keywords: graphene oxide; lignin; hybrid nanocomposite; additive manufacturing

Check for updates

Academic Editor: Candido Fabrizio Pirri

Received: 14 December 2025
Revised: 26 January 2026
Accepted: 28 April 2026
Published: 2 June 2026

Copyright: © 2026 by the authors. Licensee MDPI, Basel, Switzerland. This article is an open access article distributed under the terms and conditions of the Creative Commons Attribution (CC BY) license.

1. Introduction

Additive manufacturing processes based on photocurable resins rely on the polymerization of successive layers initiated by UV or visible radiation in a similar spectral range [1,2]. Despite their widespread use, photocurable resins used in resin-based 3D printing exhibit a well-known mechanical limitation related to their curing mechanism, which leads to dense and highly crosslinked networks that fail in a brittle manner, displaying low toughness and limited elongation at break [3,4]. This intrinsic fragility restricts their application in functional components subjected to impact, flexural stresses, or repeated mechanical

loading. Such behavior is primarily related to the widespread use of multifunctional acrylate monomers, which promote high crosslink densities [4–6]. Although commercially available flexible formulations, often based on polyurethane- or epoxy-acrylate systems, can improve deformability, they typically do so at the expense of elastic modulus, limiting their suitability for applications requiring stiffness and dimensional stability [6–8]. Consequently, alternative strategies have been extensively investigated to overcome this inherent balance between toughness and stiffness, among which the incorporation of nanofillers has emerged as a prominent approach to enhance the mechanical performance of SLA-printed parts [1,9].

A wide range of nanofillers has been evaluated in photocurable resins, including nanosilica, nanoclay, graphene, and their derivatives [10–13]. Among these, graphene oxide (GO) has attracted particular attention due to its high specific surface area and abundant oxygen-containing functional groups, which impart polarity to the nanosheets and favor interactions with polar resin matrices. Several studies have demonstrated that GO can effectively modulate the mechanical response and introduce additional functionalities in photocurable systems, even at low loadings [14–16]. Despite this potential, its use in photocurable resins is often limited by the strong tendency of the sheets to reaggregate during formulation and curing [14,15]. This behavior reduces dispersion stability and promotes the formation of agglomerates, which ultimately compromises the cohesion and mechanical performance of 3D-printed nanocomposites [17,18].

Armentia et al. [13] examined the influence of graphene-based nanomaterials on the photopolymerization behavior and printability of an acrylic resin used in SLA. Incorporating 0.1 wt.% of graphene, GO or graphite nanoplatelets (GoxNP) produced material-dependent effects: GO and GoxNP maintained good dispersion, preserved light penetration and yielded printed parts with normal curing behavior, while graphene increased light absorption, lowered the degree of cure and compromised printability. Shah et al. [14] investigated how GO dispersion affects the mechanical and thermal properties of 3D-printed nanocomposites. Tensile and compression strength were highest at 0.05 wt.% GO and gradually decreased at higher loadings (0.05–0.5 wt.%), while thermal stability was largely unaffected. In a previous study from our group [18], we evaluated the influence of GO addition on the mechanical behavior of acrylated resin nanocomposites subjected to multiple loading conditions and fabricated by SLA printing. At a GO content of 0.5 wt.%, the experimental results showed good agreement with the Drucker–Prager theoretical model. At higher GO concentrations, however, deviations from the model were observed, which were attributed to the influence of GO agglomerates on the material flow behavior. These results indicate that while GO is a promising reinforcement, its effective use in photocurable resins requires strategies to improve dispersion and interfacial compatibility.

In this context, lignin has emerged as a promising candidate to improve GO dispersion and stabilization within resin matrices. The aromatic structure of lignin enables π–π interactions with GO, while its oxygen-rich and highly functionalized backbone can enhance compatibility with photocurable systems [19,20]. Lignins are natural polyphenols formed through the polymerization of monolignols, including coniferyl, sinapyl, and p-coumaryl alcohols, which give rise to molecular units of guaiacyl (G), sinapyl (S), and p-hydroxyphenyl (H), respectively [21,22]. In plant cell walls, lignin plays a key structural role, contributing to mechanical integrity and growth [21].

On this basis, Hu et al. [20] reported the preparation of GO-alkaline lignin (AL) nanohybrids and their reinforcing effect in poly(vinyl alcohol) (PVA) composites. The GO–AL nanohybrids exhibited good dispersion stability in aqueous media, enabling effective incorporation into the polymer matrix. As a result, PVA composites containing GO–AL showed

significantly enhanced mechanical performance compared to systems reinforced with GO or AL alone, highlighting the synergistic role of lignin in GO-based hybrid reinforcements.

Despite its abundance and chemical versatility [23], the application of lignin in polymer systems is often constrained by its inherent structural heterogeneity and broad molecular weight distribution, which depend strongly on botanical origin and pulping process [21,24,25]. These factors define the properties of technical lignins (TL), obtained as by-products of cellulose pulping. To address these limitations, increasing attention has been directed toward lignin fractionation strategies aimed at isolating fractions with narrower molecular weight distributions and improved processability [26,27]. In particular, low-molecular-weight lignin fractions exhibit higher mobility and greater accessibility of functional groups, enhancing their reactivity and compatibility in polymer blends and composites [28]. Among the various approaches reported, sequential solvent extraction remains one of the most widely adopted methods due to its simplicity and low cost [26,29,30].

This work investigates the co-incorporation of GO and lignin, as well as a low-molecular-weight fraction, in acrylate-based resins processed by SLA, to evaluate how these hybrid systems affect the mechanical and viscoelastic performance of the resulting photocurable materials. The role of lignin molecular weight is examined in terms of its influence on the structure–property relationships governing the thermomechanical response of the resulting 3D-printed parts. Although several studies have independently assessed the effects of GO [7,16,18,31] or lignin [32–34] in photocurable nanocomposites, to the best of our knowledge, this is the first work to examine this hybrid system in photopolymer resins. By demonstrating how lignin and its low-molecular-weight fraction modulate the mechanical and viscoelastic behavior of GO-containing systems, this study advances the understanding of hybrid systems in photocurable resins and introduces a novel approach for tailoring the properties of SLA-produced nanocomposites.

2. Materials and Methods

2.1. Materials

Graphite (Grafine 996100) was supplied by Nacional de Grafite (Salto da Divisa, Brazil). Sulfuric acid (H_2SO_4), phosphoric acid (H_3PO_4), and hydrochloric acid (HCl) were purchased from Labsynth (Diadema, Brazil). Tetrahydrofuran (THF) and ethyl acetate were obtained from Êxodo Científica (Sumaré, Brazil), while potassium permanganate ($KMnO_4$) and hydrogen peroxide (H_2O_2) were acquired from Sigma-Aldrich (São Paulo, Brazil). Kraft lignin derived from eucalyptus hardwood was provided by Suzano S.A. (Suzano, Brazil) as a brown powder, a byproduct of the pulp and paper industry, with a pH of 3.5 and an ash content of 2%. The hybrid composites were prepared using a standard acrylate-based resin supplied by 3D Cure (Betim, Brazil). The resin is transparent, has a density of 1.1 g/cm^3, and exhibits an absorption band centered at 405 nm. All reagents were used as received.

2.2. Synthesis of Graphene Oxide and Lignin Fractionation

Graphene oxide (GO) was synthesized following a modified Hummers-type method, as described by Marcano et al. [35]. Briefly, graphite (3 g) was dispersed in a mixed acid solution composed of H_2SO_4 and H_3PO_4 (9:1 *v*:*v*) under continuous stirring at 25 °C. Potassium permanganate (18 g) was then gradually introduced into the suspension, after which the reaction mixture was heated to 50 °C and maintained under agitation for 12 h. Upon completion, the reaction was allowed to cool to 25 °C and subsequently quenched by slow addition into 400 mL of ice, followed by the addition of 3 mL of a 30% H_2O_2 solution. The resulting suspension was centrifuged at 4000 rpm for 4 h to separate the solid product. The collected solid was washed sequentially with distilled water (200 mL) and a 30% HCl

solution, followed by two additional washing steps using ethanol. After each washing step, centrifugation was performed at 4000 rpm for 4 h. Finally, the product was coagulated in 200 mL of ether and dried under vacuum at 80 °C overnight.

The lignin fractionation procedure employed in this study was established based on the work of Araújo et al. [36], aiming at the recovery of a KL fraction with low molar mass and reduced dispersity. Briefly, 5 g of kraft lignin (KL) was stirred with 100 mL of ethyl acetate for 2 h at 25 °C. The mixture was then subjected to vacuum filtration, and the soluble fraction was recovered by solvent evaporation. The obtained fraction (FKL) was dried in a vacuum oven at 60 °C for 24 h to remove residual solvent and moisture.

2.3. Characterization Methods for GO and Lignin

X-ray diffraction (XRD) analyses were performed to characterize pristine graphite and graphene oxide (GO). The diffraction patterns were collected using a Bruker D8-Focus diffractometer (Billerica, MA, USA) equipped with a Cu Kα radiation source (λ = 1.54 Å). Measurements were carried out over a 2θ range from 5° to 30°, employing a scanning rate of 1°/min.

Fourier-transform infrared (FTIR) spectroscopy analyses of GO, KL, and FKL were conducted in attenuated total reflection (ATR) mode using a Perkin Elmer Spectrum Two spectrometer (Hopkinton, MA, USA). A total of 64 scans were collected in the range of 4000–700 cm^{-1} with a resolution of 4 cm^{-1}.

The molar mass distribution of KL and FKL was evaluated by gel permeation chromatography (GPC). The lignin samples were dissolved at a concentration of 2.5 mg/mL in a sodium phosphate solution adjusted to pH 12 to ensure adequate solubilization. The analyses were performed using PSS MCX columns (PSS (Polymer Standards Service) GmbH, Mainz, Germany) with nominal pore sizes of 1000 Å and 100,000 Å (8 × 300 mm), maintained at 25 °C. To evaluate the effects of sample preparation and storage on the chromatographic response, four analytical conditions were examined. The samples were either homogenized, filtered through a 0.22 µm PVDF membrane, and injected immediately, or stirred at 270 rpm for 30 min prior to filtration and injection. Additionally, reinjections were performed after 4 h of storage in the autosampler at 20 °C and after 30 days of refrigerated storage. All analyses were carried out using a flow rate of 0.6 mL/min and an injection volume of 20 µL. Detection was performed using an ultraviolet detector operating at a wavelength of 215 nm.

2.4. SLA Resin Preparation and 3D Printing

The preparation of photocurable resins containing GO and lignin, based on studies by Palaganas et al. [37] and Garcia et al. [18], was carried out in two main steps: dispersion of GO and KL or FKL, followed by their incorporation into the resin. Dispersion was performed using THF as solvent. GO, KL, and FKL were dispersed separately in THF using an ultrasonic bath for 30 min. Subsequently, GO was combined with KL or FKL and the mixture was further sonicated for an additional 30 min. The GO–KL or GO–FKL dispersions were then incorporated into the photocurable resin, and the systems were maintained at 60 °C under stirring for 12 h to allow complete evaporation of THF. The neat resin was subjected to the same THF addition and evaporation procedure to eliminate potential solvent-related effects. The GO concentration was fixed at 0.5 wt.% based on a previous study [18], which identified this loading as optimal in terms of dispersion and processability for photocurable resin systems. The concentrations of KL and FKL were then defined relative to the GO content, establishing GO:lignin ratios of 1:0.5, 1:1, and 1:2. This notation was adopted in the sample nomenclature, followed by the identification of the lignin type used (KL or FKL).

The samples were printed using an Anycubic Photon Mono 4K printer (Shenzhen, China), operating at a wavelength of 405 nm. The first six layers were exposed to UV light for 120 s to enhance adhesion to the build platform, while subsequent layers were exposed for 30 s, with a layer thickness of 0.05 mm. Depending on the specimen thickness, the total printing time ranged from approximately 30 to 40 min. After printing, the specimens were washed with ethanol to remove uncured resin residues. The samples were then post-cured in a UV curing chamber equipped with a 405 nm light source for 20 min and subsequently subjected to a vacuum oven at 90 °C for 24 h to complete the cross-linking process.

2.5. Characterization of Hybrid Nanocomposites

In the uncured state, the dispersion of GO and lignin in the hybrid system, as well as the viscosity of the formulations, were evaluated by optical microscopy and rheometry, respectively. For micrograph acquisition, a small amount of each sample was placed between glass slides and gently pressed using tweezers. The micrographs were obtained using a Carl Zeiss Axio Scope A1 optical microscope (Oberkochen, Germany).

The viscosity of the mixtures was evaluated using a rotational rheometer Anton Paar MCR 502 (Graz, Austria), employing a parallel plate geometry with a diameter of 25 mm and a gap of 0.2 mm, based on previous studies [18,34]. Measurements were carried out at 25 °C, with a shear rate sweep ranging from 1 to 100 s^{-1}.

The sedimentation stability of the uncured resin formulations was evaluated by visual monitoring over time. Aliquots of each formulation were transferred to 3 mL glass vials and kept under static conditions at 25 °C. The samples were visually inspected at predetermined time intervals ranging from 1 h up to 72 h to assess possible particle sedimentation.

After curing, the mechanical properties of the samples were assessed by tensile tests performed on a universal testing machine Instron 3369 (Norwood, MA, USA), equipped with a 50 kN load cell. The tests were conducted using an optical extensometer and a crosshead speed of 2 mm/min. Dumbbell-shaped specimens were used, with a gauge length of 25 mm, gauge width of 5 mm, and thickness of 2 mm, in accordance with ISO 527-2 [38].

The viscoelastic properties of the hybrid nanocomposites were investigated by dynamic mechanical analysis (DMA) using a TA Instruments Q800 (Waltham, MA, USA). The analyses were carried out in dual cantilever mode, at a frequency of 1 Hz and a deformation amplitude of 5 μm. Rectangular specimens were used, with a gauge length of 35 mm, width of 12 mm, and thickness of 3 mm. The temperature ramp was conducted from 20 to 140 °C at a heating rate of 5 °C/min.

FTIR-ATR spectroscopy was employed to evaluate the curing behavior of the resin formulations before and after UV exposure. The analyses were performed using a PerkinElmer Spectrum Two spectrometer (Hopkinton, MA, USA). A total of 64 scans were collected in the range of 4000–550 cm^{-1} with a resolution of 4 cm^{-1} for each sample.

The fracture surfaces of the tensile-tested samples were coated with a thin layer of gold (15 nm) and examined by scanning electron microscopy (SEM) using a Jeol JSM-6010LA microscope (Akishima, Japan), operated at acceleration voltages between 5 and 15 kV.

3. Results and Discussion

3.1. Characterization of GO and Lignin

3.1.1. Graphene Oxide

The X-ray diffraction patterns of pristine graphite and GO are presented in Figure 1. Pristine graphite exhibits an intense diffraction peak at $2\theta = 26.6°$, characteristic of the (002) reflection, corresponding to an interplanar spacing (d) of 3.3 Å [39].

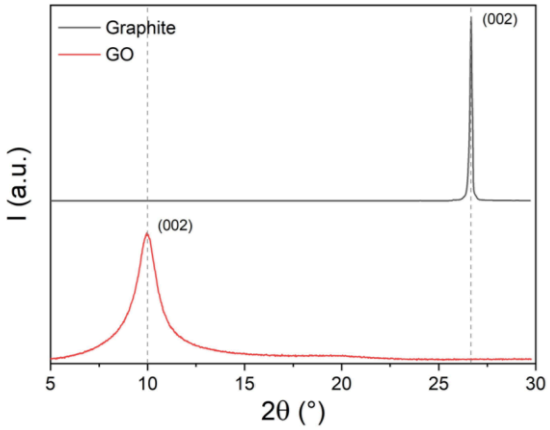


Figure 1. XRD pattern of pristine graphite and GO.

After the oxidation process, a pronounced shift in this reflection toward lower diffraction angles is observed, with the (002) peak of GO located at 2θ = 10°, corresponding to an interlayer spacing of 8.8 Å. This increase in interplanar distance is mainly associated with the introduction of oxygen-containing functional groups, which promotes layer expansion, while a minor contribution from interlayer water is also expected as a result of the increased hydrophilicity of the obtained GO [40]. In addition, a weak peak is observed at 2θ ≈ 20°, indicating the presence of a small fraction of graphene sheets that were not fully oxygen-functionalized during the oxidation process [41].

The FTIR spectrum of GO (Figure 2) exhibits the characteristic absorption bands associated with this nanomaterial, confirming the presence of multiple oxygen-containing functional groups. A broad band centered at approximately 3250 cm^{-1} is observed, which is attributed to the stretching vibrations of hydroxyl (–OH) groups, indicating a high degree of surface functionalization. [42,43]. The absorption band located at 1728 cm^{-1} is assigned to the stretching vibration of C=O bonds from carboxylic groups, while the band around 1613 cm^{-1} corresponds to the C=C stretching vibrations of aromatic domains remaining from the graphitic structure [37].

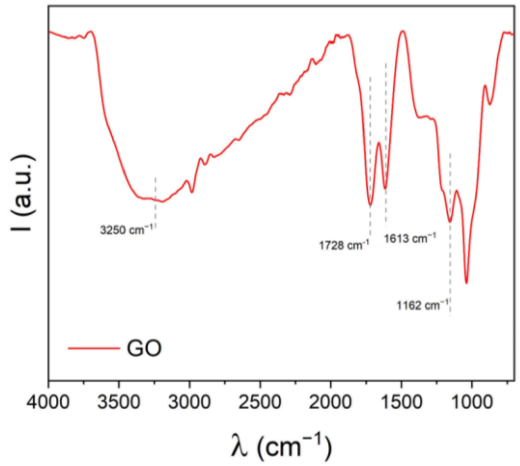


Figure 2. FTIR spectrum of GO.

Additionally, bands in the region between 1367 and 1380 cm^{-1} are associated with the deformation of C–OH groups, whereas the band at approximately 1162 cm^{-1} is attributed to the stretching vibration of C–O bonds in epoxide or alkoxy groups located on the basal plane of GO [27]. These features confirm the successful introduction of oxygenated functional

groups into the graphene structure, in agreement with the structural modifications observed by XRD, and demonstrate the effective synthesis of the GO.

3.1.2. Lignin

Figure 3 presents the FTIR-ATR spectra of KL and FKL, normalized to the intensity of the band at 1455 cm^{-1}, which is assigned to the asymmetric bending vibrations of CH_3 and CH_2 groups [21]. Overall, KL and FKL exhibit a high degree of spectral similarity. A broad band is observed in the 3650–3050 cm^{-1} region, with a maximum centered at 3398 cm^{-1}, which is attributed to the stretching vibrations of hydroxyl (–OH) groups from both aromatic and aliphatic structures. The bands at 2937 and 2845 cm^{-1} are assigned to C–H stretching vibrations of methylene and methyl groups [21,36]. The band located at 1718 cm^{-1} is attributed to the stretching vibration of the C=O bond, mainly associated with carboxylic and conjugated carbonyl groups. The intensity of this band is slightly higher for FKL compared to KL, a trend consistent with kraft lignin fractions of lower molar mass, as reported by Araújo et al. [36]. The band at 1605 cm^{-1} is assigned to C=C stretching vibrations of aromatic rings in the lignin structure, while the band at 1509 cm^{-1} is associated with similar vibrations of the aromatic backbone. In the lower wavenumber region, the bands at 1325 and 1207 cm^{-1} are assigned, respectively, to phenolic C–OH vibrations and to C–O stretching vibrations in guaiacyl units. The band observed at 1106 cm^{-1} is attributed to in-plane C–H deformations of the aromatic skeleton in syringyl units, combined with C–O stretching vibrations, typically reported for kraft lignin structures [21,44].

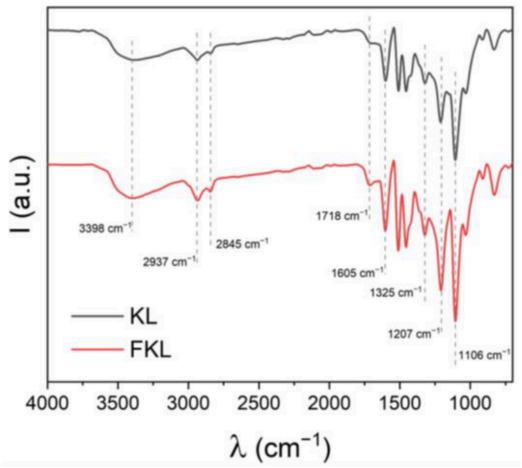


Figure 3. FTIR spectra of KL and FKL.

Table 1 presents the weight-average molar mass (M_w) and polydispersity index (PDI = M_w/M_n) values obtained by GPC for KL and its ethyl acetate-soluble fraction (FKL). The M_w values observed for KL are consistent with those reported in the literature for hardwood kraft lignin [21,45]. After fractionation, FKL exhibited a significant decrease in M_w compared with KL, decreasing from 2190 to 912 g/mol, along with a pronounced reduction in PDI from 2.3 to 1.6. Similar trends of M_w and PDI reduction following solvent fractionation have been reported in the literature. Park et al. [46], in a study of milled wood lignin, reported M_w values of 8070 g/mol for the original lignin and 2410 g/mol for the ethyl acetate-soluble fraction. For an organosolv lignin, the same authors reported M_w values of 4730 and 1470 g/mol, respectively. Consistently, Araújo et al. [36] reported M_w values of 4025 g/mol for kraft lignin and 1081 g/mol for its ethyl acetate-soluble fraction. These results confirm the effectiveness of the fractionation procedure employed in this study in reducing both the average molar mass and the polydispersity of lignin.

Table 1. M_w and PDI of KL and FKL.

Sample	M_w (g/mol)	PDI
KL	2190	2.3
FKL	912	1.6

3.2. Pre-Curing Dispersion and Viscosity

Figure 4 presents optical micrographs of the dispersion of GO and of the 1:2 KL and 1:2 FKL hybrid nanocomposites. The sample containing only GO (Figure 4a) exhibits a relatively homogeneous dispersion, although the presence of aggregates distributed throughout the polymer matrix is evident. The formation of these aggregates is consistent with results reported in the literature, indicating that at this GO concentration strong interactions occur, mainly driven by van der Waals forces and π-π interactions [18,47]. In the hybrid nanocomposites, the formulation containing KL (Figure 4b) shows behavior like that observed for the GO-only sample, with a high density of aggregates. In contrast, the formulation containing FKL (Figure 4c) exhibits a clear reduction in aggregate density, indicating more efficient interactions between GO, FKL, and the acrylate matrix.

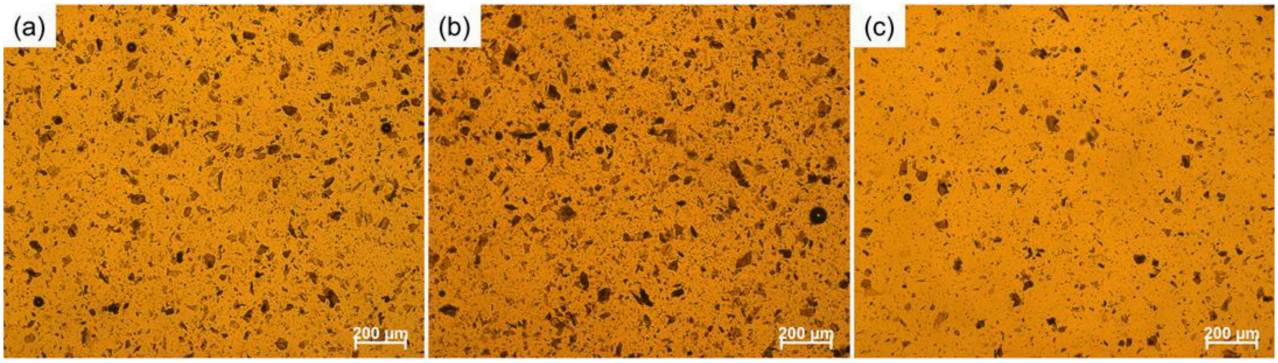


Figure 4. Optical micrographs of resin formulations containing (**a**) GO, (**b**) 1:2 KL, and (**c**) 1:2 FKL.

The dispersion of lignin in the resin is governed by its interaction with the polymer matrix [48]; however, the lower molecular weight of FKL plays a key role in this process. The reduction in molecular weight leads to increased chain mobility [22,49], which favors both stronger interactions with the matrix and more efficient intercalation between GO sheets. As a result, the GO–FKL hybrid system exhibits a more homogeneous dispersion within the photocurable resin.

Viscosity is a critical parameter in SLA-based printing, as it governs both the efficiency with which the resin recoats the previously cured surface and the time required to prepare the system for the next exposure step [33]. High viscosities delay resin flow into the volume corresponding to the cured layer, increasing the recoating time and potentially exceeding the exposure window of the subsequent layer, which can lead to defects and longer overall printing duration [18]. According to the literature, resins used for SLA printing typically operate within viscosity ranges between 200 and 1000 mPa·s [11]. Figure 5 shows the viscosity–shear rate curves for the neat resin and for the compositions containing GO and lignin, and all formulations fall within the ranges generally considered suitable for SLA processing.

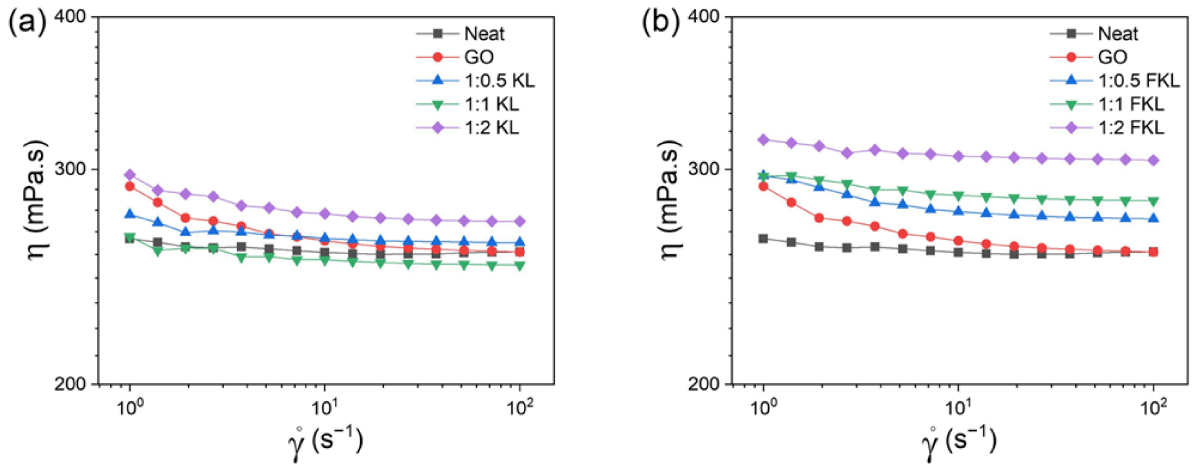


Figure 5. Viscosity of the neat resin and resin formulations incorporating (**a**) GO and (**b**) lignin.

The neat resin exhibits Newtonian behavior across the entire shear-rate range evaluated, with a viscosity of 263 mPa·s at 1 s^{-1}. The formulation containing GO presents a moderate increase in viscosity (290 mPa·s at 1 s^{-1}), suggesting effective interactions between the resin and the oxygenated functional groups present on GO [50]. The addition of GO also induces a deviation from Newtonian behavior at low shear rates, a trend previously reported for acrylic-based nanocomposites containing GO and attributed to the formation of agglomerates within the polymer matrix [18].

The GO–KL hybrid formulations (Figure 5a) exhibit distinct responses depending on lignin concentration. At low lignin content (1:0.5 KL), only minor changes in viscosity were observed, although the formulation recovers a predominantly Newtonian profile. The 1:1 KL composition shows a decrease in viscosity relative to GO, whereas the highest lignin content (1:2 KL) results in the largest viscosity among the KL-containing formulations. The viscosities at 1 s^{-1} were 275, 264, and 297 mPa·s for the 1:0.5, 1:1, and 1:2 KL samples, respectively.

In contrast, the GO–FKL formulations (Figure 5b) show a progressive increase in viscosity as the FKL content increases, ranging from 263 to 307 mPa·s at 1 s^{-1}. All FKL-containing samples exhibit higher viscosities than their corresponding KL formulations. An increase in viscosity with lignin content has been widely reported and is commonly associated with the restriction of polymer-chain mobility imposed by lignin [51]. Sutton et al. [33] similarly observed a continuous rise in viscosity upon addition of acrylate-modified lignin, increasing from 440 to 1660 mPa·s at 15 wt.%.

This overall behavior suggests favorable interactions among the resin, GO, and FKL, which are consistent with the lower molecular weight of the FKL fraction and corroborated by optical micrographs. KL, on the other hand, exerts a less pronounced influence on viscosity, with a marked increase only at the highest KL content (1:2 KL). A similar trend was reported by Ibrahim et al. [52] for graphene–lignin hybrid composites in polyurethane-based resins, where negligible viscosity changes were observed up to 3 wt.% hybrid loading.

Beyond viscosity, dispersion stability over printing time is another critical factor for SLA-based processing of reinforced systems. Sedimentation tests were therefore performed over a time interval ranging from 1 to 72 h to assess whether the formulations remain stable over time, considering the residence time of the resin inside the printer.

Figure 6 shows representative images of the uncured neat resin and of resin formulations containing GO, 1:2 KL, and 1:2 FKL as a function of time (additional time points are shown in Figure S1). All formulations exhibit good visual stability during the first hour of monitoring, which corresponds to the time required to complete the printing process. This

behavior indicates sufficient dispersion stability over the relevant printing time and, when combined with the suitable viscosity range discussed in Figure 5, suggests good potential for defect-free printing with uniformly distributed reinforcements [34]. In addition, the viscosity of these formulations was monitored over a 1 h interval and remained stable during this period (Figure S2).

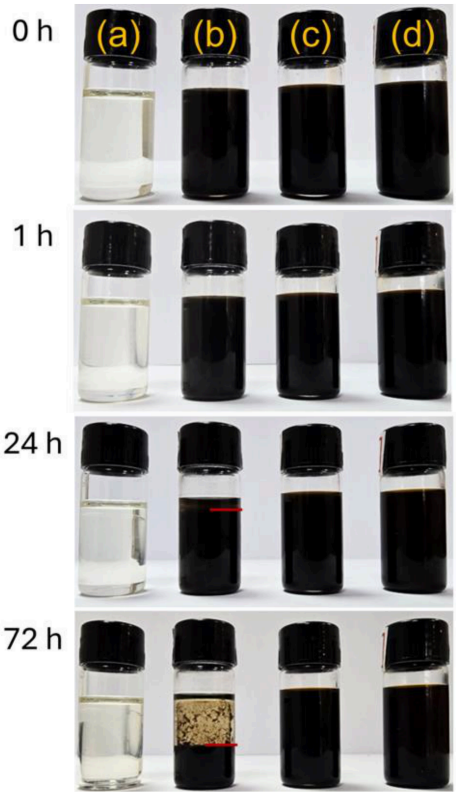


Figure 6. Visual sedimentation stability of uncured (**a**) neat resin and resin formulations containing (**b**) GO, (**c**) 1:2 KL, and (**d**) 1:2 FKL over time.

After 24 h of monitoring, slight sedimentation becomes noticeable in the formulation containing GO, as highlighted by the red marking in Figure 6, and progressively increases up to 72 h. In contrast, over the same time interval, the resin formulations containing 1:2 KL or 1:2 FKL exhibit higher visual stability, with no evident phase separation. This behavior can be attributed both to the higher viscosity of lignin-containing systems, which retards particle sedimentation, and to favorable interactions between GO and lignin, such as π–π interactions between aromatic rings and hydrogen bonding. These interactions hinder GO re-agglomeration and, consequently, delay sedimentation within the resin matrix [20,52].

3.3. Hybrid Nanocomposites

3.3.1. Mechanical Properties

Figure 7a presents the Young's modulus values obtained for the 3D-printed specimens. The neat resin exhibited the highest stiffness among all formulations, with a Young's modulus of 2.25 GPa. The incorporation of GO led to a reduction in stiffness, with the GO-only formulation reaching a modulus of 1.86 GPa, corresponding to a decrease of approximately 17% relative to the neat resin.

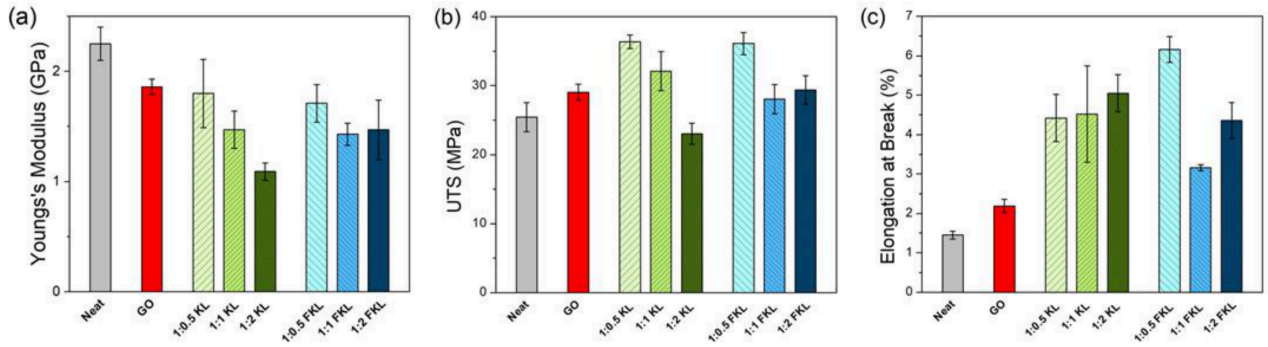


Figure 7. (**a**) Young's modulus, (**b**) ultimate tensile strength, and (**c**) elongation at break of hybrid nanocomposites containing GO and lignin.

The hybrid formulations containing lignin showed a further decrease in elastic modulus. At low lignin contents, the 1:0.5 KL and 1:0.5 FKL formulations exhibited slightly lower modulus values than the GO-only system, reaching 1.80 and 1.71 GPa, respectively. As the KL content increased, a more pronounced reduction in stiffness was observed, with the 1:2 KL formulation exhibiting the lowest Young's modulus among all tested samples. Both KL- and FKL-based nanocomposites exhibited a similar decreasing trend in elastic modulus with increasing lignin content.

The ultimate tensile strength (UTS) results for the 3D-printed nanocomposites are reported in Figure 7b. The neat resin reached about 26 MPa, while the incorporation of GO increased this value to about 29 MPa. At low lignin contents, a pronounced synergistic effect was observed between GO and lignin. Both the 1:0.5 KL and 1:0.5 FKL formulations reached UTS values close to 36 MPa, representing the highest tensile strengths among all samples and surpassing both the neat resin and the GO-only formulation. This behavior may be associated with more effective stabilization of GO at low lignin contents and a reduced tendency of the polyphenols to form agglomerates under these conditions. Similar trends were reported by Hu et al. [20], who observed a strong synergistic reinforcing effect in PVA composites containing GO–alkaline lignin hybrid fillers, with increases of 84% in tensile strength and 335% in Young's modulus at a GO–AL ratio of 1:4 and a total filler content of 4 wt.%.

As the polyphenol content increased, a progressive reduction in UTS was observed relative to the low-content formulations. Despite this decrease, most compositions still exhibited tensile strengths comparable to or higher than that of the neat resin and the GO-only system. The main exception was the 1:2 KL formulation, which showed a marked deterioration in tensile strength, decreasing to approximately 23 MPa. Overall, these results indicate that increasing lignin content leads to a gradual loss in tensile strength, while the use of the low-molecular-weight fraction mitigates this effect relative to unfractionated lignin.

The improved tensile performance of the FKL-based formulations may be related to the lower molecular weight and higher mobility of this fraction. These characteristics may favor intercalation between GO flakes, promoting more effective stabilization and limiting the formation of mixed agglomerates. In contrast, unfractionated lignin tends to aggregate more extensively at higher contents, leading to the formation of larger domains that act as stress concentration sites and ultimately reduce tensile strength. This behavior is consistent with the sharper decline in UTS observed for the KL-based formulations [32,53].

Figure 7c summarizes the elongation at break values measured for the nanocomposite formulations. The neat resin reached about 1.4%, reflecting the brittle behavior expected for highly crosslinked photocurable materials [4,5]. The incorporation of GO alone led to a modest increase in deformability, reaching around 2.2%. In comparison to GO, the addition of lignin resulted in a more substantial increase in elongation at break. The KL-based

formulations reached approximately 4.4% (1:0.5 KL), 4.5% (1:1 KL), and 5.0% (1:2 KL), while the FKL-based nanocomposites showed the highest elongation values, reaching 6.1% for 1:0.5 FKL, followed by 3.1% (1:1 FKL) and 4.3% (1:2 FKL).

Although KL and FKL are intrinsically rigid materials, their incorporation prominently increased the deformability of the 3D-printed nanocomposites, likely due to a reduction in the effective crosslink density of the resin [32,34]. These results indicate that both KL and, more prominently, FKL promote increased deformability of the 3D-printed nanocomposites, which is likely associated with increased toughness in these nanocomposites [31–33].

3.3.2. Viscoelastic Properties

Figure 8 shows the storage modulus (E′) and damping factor (tan δ = E″/E′) curves for the GO–KL (Figure 8a) and GO–FKL (Figure 8b) formulations. All samples exhibit a similar general profile, characterized by a vitreous plateau at low temperatures followed by a marked decrease associated with increased polymer-chain mobility, and finally the emergence of a rubbery plateau at approximately 100 °C. This latter region is typically associated with the crosslink density of the network [18,54]. The E′ values at 140 °C are summarized in Table 2, where a slight increase in modulus can be observed upon addition of GO. Garcia et al. [18] discussed the influence of GO on the crosslink density of an acrylate-based resin and attributed changes in modulus to two concurrent effects: a decrease in curing density, which would reduce crosslink density and thus lower E′, and the intrinsic stiffness of the nanomaterial, which tends to increase E′ relative to the polymeric matrix.

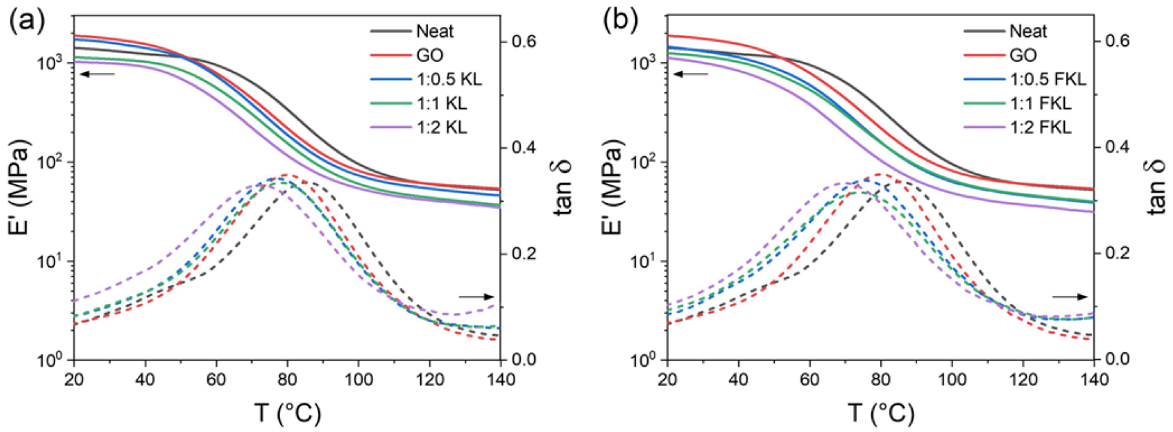


Figure 8. E′ (solid lines) and tan δ (dashed lines) curves of (**a**) GO-KL and (**b**) GO-FKL hybrid nanocomposites.

Table 2. Values of Storage modulus (E′) and T_g from DMA.

Sample	T_g (°C)	E′ at 140 °C (MPa)
Neat	85.4	52.7
GO	80.8	53.1
1:0.5 KL	76.8	46.0
1:1 KL	77.8	37.1
1:2 KL	71.5	34.7
1:0.5 FKL	75.8	38.8
1:1 FKL	73.1	39.8
1:2 FKL	70.0	31.0

For the hybrid GO–lignin nanocomposites, a clear decrease in E′ is observed as lignin content increases, reaching 34.7 and 31.0 MPa for the KL- and FKL-containing formulations, respectively, compared with 52.7 MPa for the neat resin. This decreasing trend is noteworthy,

particularly because lignin is intrinsically rigid and has often been associated with increases in E′ when incorporated into polymer matrices [55]. In this system, however, the observed reduction indicates a decrease in crosslink density. A similar conclusion was drawn by Zhang et al. [32] when examining a commercial methacrylate resin reinforced with softwood kraft lignin, where a decrease in crosslink density was attributed to the UV-absorbing capability of lignin.

The tan δ curves provide insight into polymer-chain mobility, with the peak position corresponding to the glass transition temperature (T_g), reported in Table 2. The neat resin exhibits a T_g of 85.4 °C, which decreases to 80.8 °C upon addition of GO. The hybrid nanocomposites show a continuous decrease in T_g with increasing lignin content, an effect more pronounced for the FKL formulations, with T_g values of 71.5 and 70.0 °C for the 1:2 KL and 1:2 FKL samples, respectively. In polymer composites, a classical mechanism involves an increase in T_g due to reduced chain mobility induced by rigid fillers, behavior that has also been reported in lignin-containing systems [48,56]. However, similar T_g reductions have been previously observed in SLA systems. Colucci et al. [34] reported a decrease in T_g from 15 to 10 °C upon addition of 10 phr of softwood kraft lignin to a soybean-oil-based resin, which was attributed to a reduction in crosslink density. This interpretation aligns with the trends observed in the rubbery plateau as well as with the mechanical behavior, where decreases in elastic modulus and increases in deformability were detected.

The more pronounced T_g reduction observed for the FKL-containing samples can be rationalized by the lower molecular weight of FKL, which promotes improved interaction with the polymer matrix, as supported by the optical micrographs and viscosity data, while providing a reduced ability to restrict polymer-chain mobility when compared with the higher-molecular-weight KL.

3.3.3. Curing Conversion Analysis

The degree of cure of the resin formulations containing GO and lignin was evaluated by FTIR spectroscopy. Figure 9 presents the FTIR spectra of the neat resin as well as of the formulations containing GO and the highest lignin contents (1:2 KL and 1:2 FKL), analyzed in both the uncured and cured states.

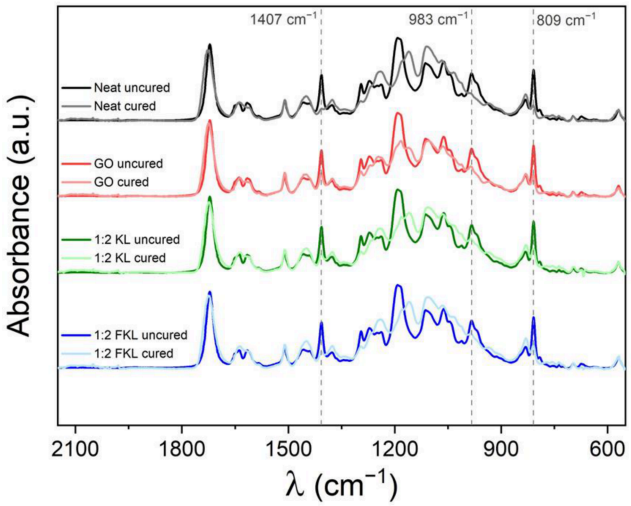


Figure 9. FTIR spectra of uncured and cured neat resin and resin formulations containing GO, 1:2 KL, and 1:2 FKL.

The FTIR spectra display the characteristic bands of the acrylic resin, with prominent absorptions associated with ester groups at 1727 cm^{-1} (C=O), 1638 cm^{-1} (C=C), and 1160 cm^{-1} (C–O–C) [13]. The incorporation of GO and lignin does not result in significant

changes in the overall spectral profile of the resin, which can be attributed to peak overlap among the components and to the relatively low concentration of the nanofillers. Similar observations have been reported for photocurable resins containing lignin at concentrations up to 3 wt.% [51].

The influence of the fillers on the curing process can be assessed by monitoring the decrease in the absorption bands associated with vinyl double bonds (=CH_2), located at 1407, 983, and 809 cm^{-1}, as highlighted in Figure 9. The degree of conversion (*DC*) was estimated by tracking the reduction in the absorbance ratio between the band at 809 cm^{-1} (A_{809}) and the ester carbonyl band at 1727 cm^{-1} (A_{1727}) before and after curing, according to Equation (1) [51]:

$$DC(\%) = \frac{(A_{809}/A_{1727})_u - (A_{809}/A_{1727})_c}{(A_{809}/A_{1727})_u} \times 100, \quad (1)$$

where the subscripts *u* and *c* refer to the uncured and cured states, respectively.

The neat resin exhibits a *DC* of 93%, in agreement with values previously reported in the literature [51]. Upon incorporation of GO, the *DC* decreases to 86.8%, indicating a partial inhibition of the photopolymerization process. The hybrid formulations containing lignin show *DC* values comparable to that of the GO-containing system, with values of 87.3% and 88.0% for the 1:2 KL and 1:2 FKL samples, respectively.

The reduction in *DC* observed upon addition of GO and lignin can be attributed to the ability of both components to absorb UV radiation, thereby competing with the photopolymerization process [13,51]. This effect is consistent with the decrease in T_g observed by DMA (Table 2) and supports the interpretation of a reduced effective crosslink density. Importantly, the incorporation of lignin into the GO-containing formulations does not lead to a further decrease in DC, indicating that the mechanical trends observed for the hybrid nanocomposites are not primarily governed by incomplete curing, but rather by the synergistic interaction between GO and lignin within the cured network.

3.3.4. Fracture Surface

Figure 10 presents the fracture surfaces of the neat resin and the hybrid nanocomposites. The neat resin exhibits a typical brittle fracture behavior, with a relatively smooth surface and crack propagation features across the microstructure [14]. The fracture surface of the sample containing only GO (Figure 10b) exhibits the coexistence of cleavage planes and localized deformation bands, indicating a transition from the typically brittle behavior of the acrylic resin to a semi-ductile regime [18]. This effect is associated with the presence of GO sheets, which interfere with crack propagation by promoting crack deflection and branching, thereby increasing energy dissipation during fracture [57,58]. GO agglomerates can also be observed within the polymer matrix, as indicated by the arrows.

A similar morphology is observed for the hybrid nanocomposite containing a low lignin content (1:0.5 KL, Figure 10c). However, at higher KL contents (1:2 KL, Figure 10d) and in the FKL-containing formulations (Figure 10e,f), the fracture surfaces display a lower prevalence of well-defined cleavage planes and a higher density of shear bands. These features indicate an increased capacity for energy dissipation prior to fracture and suggest a greater contribution of plastic deformation mechanisms compared with brittle fracture. The more pronounced shear-banding observed for the FKL-containing samples is consistent with the enhanced chain mobility inferred from the DMA results.

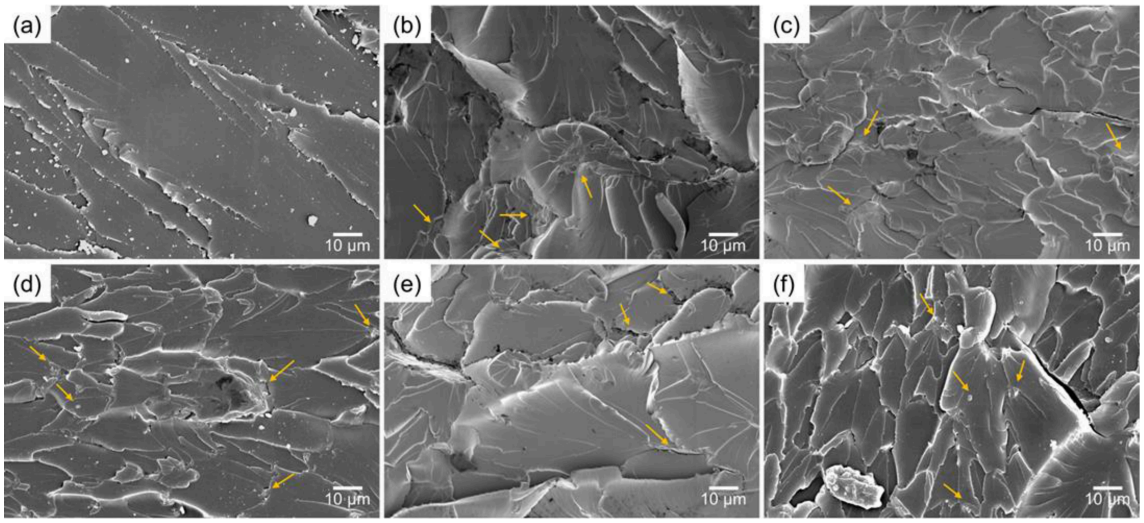


Figure 10. SEM micrographs of fracture surface of (**a**) neat resin and hybrid nanocomposites containing (**b**) GO, (**c**) 1:0.5 KL, (**d**) 1:2 KL, (**e**) 1:0.5 FKL, and (**f**) 1:2 FKL. Arrows indicate GO agglomerates.

In addition, the hybrid nanocomposites exhibit a lower apparent density of GO agglomerates, as indicated by the arrows, which is consistent with the improved dispersion stability discussed previously and supports the role of GO–lignin interactions in hindering GO re-agglomeration. Overall, the fracture surface morphology agrees well with the mechanical performance, particularly the increased elongation at break and higher tensile strength observed for the FKL formulations, indicating a more effective interaction among the components within the hybrid nanocomposite.

4. Conclusions

This work investigated the co-incorporation of graphene oxide (GO) and kraft lignin, including a low-molecular-weight lignin fraction (FKL), into acrylate-based photocurable resins processed by stereolithography. By combining structural, rheological, mechanical, and viscoelastic analyses, this study provides a comprehensive assessment of how hybrid GO–lignin systems influence both processing behavior and the resulting performance of SLA-printed materials.

Structural characterization confirmed the successful synthesis of GO and highlighted the effective fractionation of kraft lignin, yielding a fraction with significantly reduced molar mass and polydispersity. Pre-curing analyses demonstrated that all formulations maintained viscosities within ranges suitable for SLA processing, while optical microscopy revealed that the presence of FKL promoted a more homogeneous dispersion of GO compared with unfractionated lignin. This behavior was attributed to the lower molecular weight and higher mobility of FKL, which favor interactions with both the resin matrix and GO sheets. In addition, resin formulations containing GO–lignin hybrids exhibited improved dispersion stability over time compared with the formulation containing only GO, further indicating enhanced interactions within the hybrid system.

Mechanical testing showed that low lignin contents produced a pronounced synergistic effect with GO, leading to substantial improvements in tensile strength while maintaining acceptable stiffness. Although increasing lignin content resulted in reduced elastic modulus, a marked enhancement in elongation at break was observed, particularly for FKL-containing formulations. These trends were corroborated by DMA results, which revealed a reduction in effective crosslink density and glass transition temperature, as well as by fracture surface analysis. These findings were further supported by FTIR spectroscopy, which indicated similar degrees of conversion among the nanocomposites, reinforcing that

the observed mechanical performance arises from synergistic interactions within the hybrid system rather than from differences in curing efficiency.

Overall, this study demonstrates that the use of a low-molecular-weight lignin fraction represents an effective strategy to tailor dispersion, mechanical response, and toughness in GO-containing photocurable resins, while preserving printability. These findings highlight the potential of hybrid GO–lignin systems as a versatile approach for designing advanced SLA materials with balanced mechanical performance and enhanced functionality.

Supplementary Materials: The following supporting information can be downloaded at: https://www.mdpi.com/article/10.3390/nanomanufacturing6020013/s1; Figure S1: Visual sedimentation stability of uncured resin formulations; Figure S2: Time-dependent viscosity measurements.

Author Contributions: Conceptualization, R.R.d.S.J., G.E.S.G., L.G.d.F. and D.F.d.A.F.; methodology, R.R.d.S.J., G.E.S.G., L.G.d.F., D.F.d.A.F., G.R.O.d.A.T. and W.S.d.S.; software, R.R.d.S.J., G.E.S.G., L.G.d.F. and W.S.d.S.; validation, R.R.d.S.J., G.E.S.G. and D.J.d.S.; formal analysis, R.R.d.S.J., G.E.S.G., L.G.d.F., D.F.d.A.F. and G.R.O.d.A.T.; investigation, R.R.d.S.J., G.E.S.G. and L.G.d.F.; resources, R.R.d.S.J. and D.J.d.S.; data curation, R.R.d.S.J., G.E.S.G., L.G.d.F. and D.F.d.A.F.; writing—original draft preparation, R.R.d.S.J., G.E.S.G., L.G.d.F., D.F.d.A.F., G.R.O.d.A.T. and W.S.d.S.; writing—review and editing, R.R.d.S.J., G.E.S.G., L.G.d.F. and D.J.d.S.; visualization, R.R.d.S.J. and D.J.d.S.; supervision, R.R.d.S.J. and D.J.d.S.; project administration, R.R.d.S.J. and D.J.d.S. All authors have read and agreed to the published version of the manuscript.

Funding: This research received no external funding.

Data Availability Statement: The data that support the findings of this study are available from the corresponding author upon reasonable request.

Acknowledgments: The authors acknowledge the Multiuser Central Facilities (UFABC) for their experimental support.

Conflicts of Interest: Gustavo Ryoo Oliveira de Andrade Tanobe is an employee of Suzano SA. The remaining authors declare that the research was conducted in the absence of any commercial or financial relationships that could be construed as a potential conflict of interest.

References

1. Lee, T.; Kim, J.-H.; Ng, C.S.; Andreu, A.; Kim, I.; Lee, W.; Kim, H.; Su, P.-C.; Yoon, Y.-J. Prediction of Curing Depth Dependence on CNT Nanofiller Dispersion for Vat Photopolymerization 3D Printing. *Chem. Eng. J.* **2024**, *482*, 149110. [CrossRef]
2. Park, H.K.; Shin, M.; Kim, B.; Park, J.W.; Lee, H. A Visible Light-Curable yet Visible Wavelength-Transparent Resin for Stereolithography 3D Printing. *NPG Asia Mater.* **2018**, *10*, 82–89. [CrossRef]
3. Voet, V.S.D.; Strating, T.; Schnelting, G.H.M.; Dijkstra, P.; Tietema, M.; Xu, J.; Woortman, A.J.J.; Loos, K.; Jager, J.; Folkersma, R. Biobased Acrylate Photocurable Resin Formulation for Stereolithography 3D Printing. *ACS Omega* **2018**, *3*, 1403–1408. [CrossRef]
4. Riccio, C.; Civera, M.; Grimaldo Ruiz, O.; Pedullà, P.; Rodriguez Reinoso, M.; Tommasi, G.; Vollaro, M.; Burgio, V.; Surace, C. Effects of Curing on Photosensitive Resins in SLA Additive Manufacturing. *Appl. Mech.* **2021**, *2*, 942–955. [CrossRef]
5. Korhonen, H.; Sinh, L.H.; Luong, N.D.; Lehtinen, P.; Verho, T.; Partanen, J.; Seppälä, J. Fabrication of Graphene-Based 3D Structures by Stereolithography. *Phys. Status Solidi Appl. Mater. Sci.* **2016**, *213*, 982–985. [CrossRef]
6. Quan, H.; Zhang, T.; Xu, H.; Luo, S.; Nie, J.; Zhu, X. Photo-Curing 3D Printing Technique and Its Challenges. *Bioact. Mater.* **2020**, *5*, 110–115. [CrossRef] [PubMed]
7. Tsang, C.H.A.; Zhakeyev, A.; Leung, D.Y.C.; Xuan, J. GO-Modified Flexible Polymer Nanocomposites Fabricated via 3D Stereolithography. *Front. Chem. Sci. Eng.* **2019**, *13*, 736–743. [CrossRef]
8. Golubović, Z.; Danilov, I.; Bojović, B.; Petrov, L.; Sedmak, A.; Mišković, Ž.; Mitrović, N. A Comprehensive Mechanical Examination of ABS and ABS-like Polymers Additively Manufactured by Material Extrusion and Vat Photopolymerization Processes. *Polymers* **2023**, *15*, 4197. [CrossRef] [PubMed]
9. Hsiao, H.-H.; Rahmadiawan, D.; Shi, S.-C. Enhanced Tribological and Corrosion Behavior of PMMA Composites Reinforced with Surface-Modified Silica Nanoparticles and Self-Assembled Lignin Hybrid Fillers. *J. Polym. Res.* **2025**, *32*, 270. [CrossRef]
10. Ader, F.; Sharifzadeh, E. Rheological and Mechanical Behavior of Blend-Based Polymer Nanocomposites Containing Janus and Non-Janus Silica Nanoparticles. *Colloid Polym. Sci.* **2021**, *299*, 1843–1852. [CrossRef]

11. Feng, Z.; Li, Y.; Xin, C.; Tang, D.; Xiong, W.; Zhang, H. Fabrication of Graphene-Reinforced Nanocomposites with Improved Fracture Toughness in Net Shape for Complex 3D Structures via Digital Light Processing. *C* **2019**, *5*, 25. [CrossRef]
12. Alsaadi, M.; Hinchy, E.P.; McCarthy, C.T.; Moritz, V.F.; Portela, A.; Devine, D.M. Investigation of Thermal, Mechanical and Shape Memory Properties of 3D-Printed Functionally Graded Nanocomposite Materials. *Nanomaterials* **2023**, *13*, 2658. [CrossRef] [PubMed]
13. de Armentia, S.L.; Fernández-Villamarín, S.; Ballesteros, Y.; del Real, J.C.; Dunne, N.; Paz, E. 3D Printing of a Graphene-Modified Photopolymer Using Stereolithography for Biomedical Applications: A Study of the Polymerization Reaction. *Int. J. Bioprinting* **2022**, *8*, 503. [CrossRef]
14. Shah, M.; Ullah, A.; Azher, K.; Ur Rehman, A.; Akturk, N.; Juan, W.; Tüfekci, C.S.; Salamci, M.U. The Influence of Nanoparticle Dispersions on Mechanical and Thermal Properties of Polymer Nanocomposites Using SLA 3D Printing. *Crystals* **2023**, *13*, 285. [CrossRef]
15. Tilve-Martinez, D.; Neri, W.; Horaud, D.; Vukadinovic, N.; Berton, B.; Desmedt, A.; Yuan, J.; Poulin, P. Graphene Oxide Based Transparent Resins For Accurate 3D Printing of Conductive Materials. *Adv. Funct. Mater.* **2023**, *33*, 2214954. [CrossRef]
16. Uysal, E.; Çakir, M.; Ekici, B. Graphene Oxide/Epoxy Acrylate Nanocomposite Production via SLA and Importance of Graphene Oxide Surface Modification for Mechanical Properties. *Rapid Prototyp. J.* **2021**, *27*, 682–691. [CrossRef]
17. Lin, D.; Jin, S.; Zhang, F.; Wang, C.; Wang, Y.; Zhou, C.; Cheng, G.J. 3D Stereolithography Printing of Graphene Oxide Reinforced Complex Architectures. *Nanotechnology* **2015**, *26*, 434003. [CrossRef]
18. Garcia, G.E.S.; de Sousa Junior, R.R.; Gouveia, J.R.; dos Santos, D.J. Graphene Oxide-Based Nanocomposites for Stereolithography (SLA) 3D Printing: Comprehensive Mechanical Characterization under Combined Loading Modes. *Polymers* **2024**, *16*, 1261. [CrossRef] [PubMed]
19. Yan, L.; Huertas-Alonso, A.J.; Liu, H.; Dai, L.; Si, C.; Sipponen, M.H. Lignin Polymerization: Towards High-Performance Materials. *Chem. Soc. Rev.* **2025**, *54*, 6634–6651. [CrossRef] [PubMed]
20. Hu, M.; Chen, Z.; Luo, S.; Yang, X.; Ye, R.; Zheng, M.; Chen, P. Preparation of Graphene Oxide and Alkali Lignin Nanohybrids and Its Application to Reinforcing Polymer. *Wood Sci. Technol.* **2019**, *53*, 649–664. [CrossRef]
21. dos Santos, D.J.; Tavares, L.B.; Antonino, L.D.; de Sousa Junior, R.R.; Homem-de-Mello, P.; Leão, C.R. Kraft Lignin-Based Polyurethanes: Bulk Properties, Stability and Adhesion to Native Aluminum Surfaces. *Polymer* **2024**, *309*, 127457. [CrossRef]
22. Garcia, G.E.S.; Potthast, A.; Sumerskii, I.; Antonino, L.D.; de Oliveira, M.M.; de Sousa, R.R.; Rosenau, T.; dos Santos, D.J. Pyrolytic Lignin Fractionation for Rigid Polyurethane Foams: Relationship between the Pyrolysate's Chemical Structure and Foam Properties. *Sustain. Chem. Environ.* **2024**, *5*, 100065. [CrossRef]
23. Ono, K.M.; Ito, N.M.; de Sousa, R.R.; Avelino, F.; Lomonaco, D.; dos Santos, D.J. Phenolation Prior to Epoxidation of Kraft Lignin and Their Impacts on Mechanical Properties of Epoxy Adhesive. *ChemistrySelect* **2024**, *9*, e202402615. [CrossRef]
24. de Sousa Junior, R.R.; Freitas, L.P.; de Freitas, L.G.; Hubmann, T.B.; dos Santos, D.J. Hydroxypropylated Lignin as Green Tackifier in Holt-Melt Adhesive. *J. Adhes.* **2025**, *102*, 381–394. [CrossRef]
25. de Sousa Junior, R.R.; Gouveia, J.R.; Nacas, A.M.; Tavares, L.B.; Ito, N.M.; de Moura, E.N.; Gaia, F.A.; Pereira, R.F.; dos Santos, D.J. Improvement of Polypropylene Adhesion by Kraft Lignin Incorporation. *Mater. Res.* **2019**, *22*, e20180123. [CrossRef]
26. Meng, X.; Parikh, A.; Seemala, B.; Kumar, R.; Pu, Y.; Wyman, C.E.; Cai, C.M.; Ragauskas, A.J. Characterization of Fractional Cuts of Co-Solvent Enhanced Lignocellulosic Fractionation Lignin Isolated by Sequential Precipitation. *Bioresour. Technol.* **2019**, *272*, 202–208. [CrossRef]
27. Pang, T.; Wang, G.; Sun, H.; Sui, W.; Si, C. Lignin Fractionation: Effective Strategy to Reduce Molecule Weight Dependent Heterogeneity for Upgraded Lignin Valorization. *Ind. Crops Prod.* **2021**, *165*, 113442. [CrossRef]
28. Jiang, X.; Savithri, D.; Du, X.; Pawar, S.; Jameel, H.; Chang, H.; Zhou, X. Fractionation and Characterization of Kraft Lignin by Sequential Precipitation with Various Organic Solvents. *ACS Sustain. Chem. Eng.* **2017**, *5*, 835–842. [CrossRef]
29. Li, M.-F.; Sun, S.-N.; Xu, F.; Sun, R.-C. Sequential Solvent Fractionation of Heterogeneous Bamboo Organosolv Lignin for Value-Added Application. *Sep. Purif. Technol.* **2012**, *101*, 18–25. [CrossRef]
30. Song, Y.; Ji, H.; Shi, X.; Yang, X.; Zhang, X. Successive Organic Solvent Fractionation and Structural Characterization of Lignin Extracted from Hybrid Poplar by Deep Eutectic Solvent for Improving the Homogeneity and Isolating Narrow Fractions. *Renew. Energy* **2020**, *157*, 1025–1034. [CrossRef]
31. Manapat, J.Z.; Mangadlao, J.D.; Tiu, B.D.B.; Tritchler, G.C.; Advincula, R.C. High-Strength Stereolithographic 3D Printed Nanocomposites: Graphene Oxide Metastability. *ACS Appl. Mater. Interfaces* **2017**, *9*, 10085–10093. [CrossRef]
32. Zhang, S.; Li, M.; Hao, N.; Ragauskas, A.J. Stereolithography 3D Printing of Lignin-Reinforced Composites with Enhanced Mechanical Properties. *ACS Omega* **2019**, *4*, 20197–20204. [CrossRef]
33. Sutton, J.T.; Rajan, K.; Harper, D.P.; Chmely, S.C. Lignin-Containing Photoactive Resins for 3D Printing by Stereolithography. *ACS Appl. Mater. Interfaces* **2018**, *10*, 36456–36463. [CrossRef] [PubMed]
34. Colucci, G.; Sacchi, F.; Bondioli, F.; Messori, M. 3D Printing of Lignin-based Polymeric Composites Obtained Using Liquid Crystal Display as a Vat Photopolymerization Technique. *Polym. Int.* **2025**, *74*, 828–838. [CrossRef]

35. Marcano, D.C.; Kosynkin, D.V.; Berlin, J.M.; Sinitskii, A.; Sun, Z.; Slesarev, A.; Alemany, L.B.; Lu, W.; Tour, J.M. Improved Synthesis of Graphene Oxide. *ACS Nano* **2010**, *4*, 4806–4814. [CrossRef] [PubMed]
36. Araújo, L.C.P.; Yamaji, F.M.; Lima, V.H.; Botaro, V.R. Kraft Lignin Fractionation by Organic Solvents: Correlation between Molar Mass and Higher Heating Value. *Bioresour. Technol.* **2020**, *314*, 123757. [CrossRef]
37. Palaganas, J.O.; Palaganas, N.B.; Ramos, L.J.I.; David, C.P.C. 3D Printing of Covalent Functionalized Graphene Oxide Nanocomposite via Stereolithography. *ACS Appl. Mater. Interfaces* **2019**, *11*, 46034–46043. [CrossRef] [PubMed]
38. *ISO 527-2:2012*; Plastics—Determination of Tensile Properties—Part 2: Test Conditions for Moulding and Extrusion Plastics. International Organization for Standardization: Geneva, Switzerland, 2012.
39. Shen, L.; Zhang, L.; Wang, K.; Miao, L.; Lan, Q.; Jiang, K.; Lu, H.; Li, M.; Li, Y.; Shen, B.; et al. Analysis of Oxidation Degree of Graphite Oxide and Chemical Structure of Corresponding Reduced Graphite Oxide by Selecting Different-Sized Original Graphite. *RSC Adv.* **2018**, *8*, 17209–17217. [CrossRef]
40. Karnis, I.; Krasanakis, F.; Sygellou, L.; Rissanou, A.N.; Karatasos, K.; Chrissopoulou, K. Varying the Degree of Oxidation of Graphite: Effect of Oxidation Time and Oxidant Mass. *Phys. Chem. Chem. Phys.* **2024**, *26*, 10054–10068. [CrossRef] [PubMed]
41. de Souza, Z.S.B.; Pinto, G.M.; Silva, G.d.C.; Demarquette, N.R.; Fechine, G.J.M.; Sobrinho, M.A.M. Interface Adjustment between Poly(Ethylene Terephthalate) and Graphene Oxide in Order to Enhance Mechanical and Thermal Properties of Nanocomposites. *Polym. Eng. Sci.* **2021**, *61*, 1997–2011. [CrossRef]
42. Li, W.; Tang, X.-Z.; Zhang, H.-B.; Jiang, Z.-G.; Yu, Z.-Z.; Du, X.-S.; Mai, Y.-W. Simultaneous Surface Functionalization and Reduction of Graphene Oxide with Octadecylamine for Electrically Conductive Polystyrene Composites. *Carbon* **2011**, *49*, 4724–4730. [CrossRef]
43. Dehghanzad, B.; Razavi Aghjeh, M.K.; Rafeie, O.; Tavakoli, A.; Jameie Oskooie, A. Synthesis and Characterization of Graphene and Functionalized Graphene via Chemical and Thermal Treatment Methods. *RSC Adv.* **2016**, *6*, 3578–3585. [CrossRef]
44. Pandey, K.K. A Study of Chemical Structure of Soft and Hardwood and Wood Polymers by FTIR Spectroscopy. *J. Appl. Polym. Sci.* **1999**, *71*, 1969–1975. [CrossRef]
45. Gouveia, J.R.; de Sousa Júnior, R.R.; Ribeiro, A.O.; Saraiva, S.A.; dos Santos, D.J. Effect of Soft Segment Molecular Weight and NCO:OH Ratio on Thermomechanical Properties of Lignin-Based Thermoplastic Polyurethane Adhesive. *Eur. Polym. J.* **2020**, *131*, 109690. [CrossRef]
46. Park, S.Y.; Kim, J.-Y.; Youn, H.J.; Choi, J.W. Fractionation of Lignin Macromolecules by Sequential Organic Solvents Systems and Their Characterization for Further Valuable Applications. *Int. J. Biol. Macromol.* **2018**, *106*, 793–802. [CrossRef] [PubMed]
47. Vallés, C.; Young, R.J.; Lomax, D.J.; Kinloch, I.A. The Rheological Behaviour of Concentrated Dispersions of Graphene Oxide. *J. Mater. Sci.* **2014**, *49*, 6311–6320. [CrossRef]
48. de Sousa Junior, R.R.; Garcia, G.E.S.; Antonino, L.D.; Gouveia, J.R.; dos Santos, D.J.; Carastan, D.J. Dielectric Elastomers Based on SEBS Gel: The Impact of Adding Kraft Lignin on Electro-Mechanical Performance. *Express Polym. Lett.* **2024**, *18*, 561–574. [CrossRef]
49. Ji, L.; Liu, L.-Y.; Cho, M.; Karaaslan, M.A.; Renneckar, S. Revisiting the Molar Mass and Conformation of Derivatized Fractionated Softwood Kraft Lignin. *Biomacromolecules* **2022**, *23*, 708–719. [CrossRef]
50. Kausar, A.; Ahmad, I.; Eisa, M.H.; Maaza, M.; Khan, H. Manufacturing Strategies for Graphene Derivative Nanocomposites—Current Status and Fruitions. *Nanomanufacturing* **2023**, *3*, 1–19. [CrossRef]
51. Arias-Ferreiro, G.; Lasagabáster-Latorre, A.; Ares-Pernas, A.; Ligero, P.; García-Garabal, S.M.; Dopico-García, M.S.; Abad, M.-J. Lignin as a High-Value Bioaditive in 3D-DLP Printable Acrylic Resins and Polyaniline Conductive Composite. *Polymers* **2022**, *14*, 4164. [CrossRef]
52. Ibrahim, F.; Mohan, D.; Sajab, M.S.; Bakarudin, S.B.; Kaco, H. Evaluation of the Compatibility of Organosolv Lignin-Graphene Nanoplatelets with Photo-Curable Polyurethane in Stereolithography 3D Printing. *Polymers* **2019**, *11*, 1544. [CrossRef]
53. Li, Z.; Young, R.J.; Kinloch, I.A. Interfacial Stress Transfer in Graphene Oxide Nanocomposites. *ACS Appl. Mater. Interfaces* **2013**, *5*, 456–463. [CrossRef] [PubMed]
54. Demleitner, M.; Schönl, F.; Angermann, J.; Fässler, P.; Lamparth, I.; Rist, K.; Schnur, T.; Catel, Y.; Rosenfeldt, S.; Retsch, M.; et al. Influence of Block Copolymer Concentration and Resin Crosslink Density on the Properties of UV-Curable Methacrylate Resin Systems. *Macromol. Mater. Eng.* **2022**, *307*, 2200320. [CrossRef]
55. Pappa, C.P.; Cailotto, S.; Gigli, M.; Crestini, C.; Triantafyllidis, K.S. Kraft (Nano)Lignin as Reactive Additive in Epoxy Polymer Bio-Composites. *Polymers* **2024**, *16*, 553. [CrossRef] [PubMed]
56. de Sousa Júnior, R.R.; Garcia, G.E.S.; dos Santos, D.J.; Carastan, D.J. Viscoelastic Behavior of Pressure-Sensitive Adhesive Based on Block Copolymer and Kraft Lignin. *J. Adhes.* **2024**, *100*, 139–155. [CrossRef]

57. Li, J.; Wang, L.; Dai, L.; Zhong, L.; Liu, B.; Ren, J.; Xu, Y. Synthesis and Characterization of Reinforced Acrylate Photosensitive Resin by 2-Hydroxyethyl Methacrylate-Functionalized Graphene Nanosheets for 3D Printing. *J. Mater. Sci.* **2018**, *53*, 1874–1886. [CrossRef]
58. Malek-Mohammadi, H.; Majzoobi, G.H.; Payandehpeyman, J. Mechanical Characterization of Polycarbonate Reinforced with Nanoclay and Graphene Oxide. *Polym. Compos.* **2019**, *40*, 3947–3959. [CrossRef]

Disclaimer/Publisher's Note: The statements, opinions and data contained in all publications are solely those of the individual author(s) and contributor(s) and not of MDPI and/or the editor(s). MDPI and/or the editor(s) disclaim responsibility for any injury to people or property resulting from any ideas, methods, instructions or products referred to in the content.